Spectrum of Engineering Sciences
ISSN (e) 3007-3138 (p) 3007-312X Volume 3, Issue 11, 2025

SPATIOTEMPORAL URBAN THERMAL HETEROGENEITY AND MORPHOLOGY-RELATED SPATIAL ASSOCIATIONS IN A SEMI-ARID URBAN SYSTEM

Mellak Dib[*1], Anmol Dhimal[2]

[*1]*School of Environmental Science and Engineering, Hohai University, Nanjing, China*
[2]*College of Civil and Transportation Engineering, Hohai University, Nanjing, China*

[*1]mellakdib@gmail.com, [2]anmoldhimal12@gmail.com

DOI: https://doi.org/10.5281/zenodo.20285847

Keywords
Urban thermal heterogeneity; Local Climate Zones; spatial econometrics; uncertainty propagation; semi-arid climate; land surface temperature

Article History
Received: 12 September 2025
Accepted: 10 November 2025
Published: 21 November 2025

Corresponding Author: *
Mellak Dib

Abstract
Urban thermal heterogeneity in semi-arid environments is shaped by nonlinear interactions between surface energy balance, three-dimensional morphology, and land cover dynamics, yet existing studies typically treat land surface temperature (LST) as a deterministic, error-free pixel value while ignoring spatial dependence and compounded uncertainties. This study reframes urban thermal heterogeneity as a spatially autocorrelated, uncertainty-perturbed manifestation of the surface energy balance under heterogeneous morphological boundary conditions. We integrate Local Climate Zone (LCZ) taxonomy, spatial econometrics (spatial error and spatial lag models), and nested Monte Carlo block bootstrap uncertainty propagation (B=1,000) to examine housing morphology LST associations in Ain Smara, a semi-arid urban system in northeastern Algeria, using Landsat and Sentinel-2 imagery (2013 - 2023). Results show that collective housing is associated with 2.5°C higher LST than individual housing (95% CI: 1.7 - 3.3) after spatially-aware propensity score matching, with contrasts largest in the urban core. Mediation analysis reveals that NDVI (50%) and sky view factor (38%) dominate the morphological contrast, while albedo plays a minor role (17%). Spatial dependence is substantial (global Moran's I = 0.67), and ignoring it underestimates standard errors by approximately 40%. Uncertainty is dominated by spatial bootstrap (48%) and downscaling residuals (32%), not retrieval errors. Our integrated framework moves beyond deterministic "morphology drives LST" narratives toward a probabilistic, spatially explicit, and uncertainty-aware conceptualization, providing robust inference for urban heat mitigation in data-scarce regions of the Global South.

1. Introduction

Urban thermal heterogeneity in semi-arid environments arises from nonlinear interactions between surface energy balance processes, three-dimensional urban morphology, and land cover dynamics. In water-limited settings such as northeastern Algeria, low soil moisture constrains latent heat flux, shifting the surface energy budget toward sensible and ground heat storage, which makes land surface temperature (LST) exceptionally sensitive to changes in vegetation cover, albedo, and building density (Oke et al., 2021; Bouzenoune et al., 2024). Rapid urban expansion in cities like Ain Smara has

progressively replaced individual dwellings with collective housing blocks, fundamentally altering the local surface energy balance. However, most existing studies treat LST as a deterministic, error-free pixel value, ignoring compounded uncertainties from retrieval algorithms, downscaling procedures, and atmospheric corrections (Liang et al., 2024). Furthermore, urban thermal fields exhibit strong spatial autocorrelation nearby pixels share similar surface properties and microclimatic histories violating the independence assumption of ordinary least squares and inflating type I error rates (Anselin & Rey, 2023). These limitations have produced overconfident claims about morphology-LST relationships, particularly in data-scarce regions of the Global South.

To address these gaps, we adopt the Local Climate Zone (LCZ) framework as a conceptual bridge between urban morphology and climatic response (Stewart & Oke, 2012). Each LCZ is defined by measurable parameters building height, sky view factor, surface cover fractions, and thermal admittance that directly influence the partitioning of net radiation. Compact built LCZs (e.g., LCZ 2 - 3) trap longwave radiation, enhance heat storage, and reduce turbulent exchange, whereas open LCZs (e.g., LCZ 6 - 8) allow greater nocturnal cooling and higher evapotranspiration. Recent applications in semi-arid contexts have confirmed that built-type LCZs consistently exhibit higher LST than non-built classes, and that landscape pattern indices explain substantial fractions of intra-LCZ thermal variation (Ramezani et al., 2024; Zhang et al., 2025). Nevertheless, LCZ classification itself carries uncertainty, especially in semi-arid zones where spectral confusion between bare soil and built surfaces is pronounced. Most studies treat LCZ classes as deterministic predictors rather than probabilistic assignments, compounding the general neglect of uncertainty propagation.

Our theoretical framework integrates two complementary lenses. The physical lens combines surface energy balance theory with LCZ taxonomy, positing that housing morphology alters LST through systematic changes in sky view factor, albedo, vegetation cover, and thermal inertia. In collective housing (LCZ 2 - 3), reduced sky view factor traps outgoing longwave radiation, high building density enhances ground heat storage, and limited vegetation lowers latent heat flux, shifting energy toward sensible heat (Oke et al., 2021; Khamis & Abdellatif, 2025). Conversely, individual housing (LCZ 6 - 8) typically features higher sky view factor, more vegetation, and lower thermal mass, promoting cooler surface temperatures. The physical lens thus provides a mechanism-based interpretation: collective housing is associated with higher LST because it systematically alters surface energy balance components.

The statistical inference lens jointly treats spatial dependence and uncertainty propagation. Following Anselin and Rey (2023), we model LST as a spatially autocorrelated stochastic process using spatial error and spatial lag specifications. Spatial dependence is treated as a first-order structure rather than a nuisance (Hu et al., 2024). Simultaneously, we propagate pixel-wise uncertainties from emissivity estimation, atmospheric correction, and downscaling residuals through a nested Monte Carlo block bootstrap procedure (Liang et al., 2024). This dual treatment ensures that confidence intervals for the morphology-LST association reflect both measurement uncertainty and spatial dependence an integration that, to our knowledge, has not been previously implemented in urban thermal studies. The central reframing claim is that urban thermal heterogeneity is not a deterministic function of urban form but a spatially autocorrelated, uncertainty-perturbed manifestation of the surface energy balance under heterogeneous morphological boundary conditions. This unified framework moves beyond deterministic "morphology drives LST" narratives toward a probabilistic, spatially explicit, and uncertainty-aware conceptualization, providing robust inference for the housing morphology LST contrast in Ain Smara, Algeria.

2.4 Conceptual model diagram (Figure 1)

Figure 1 presents the integrated two-layer framework guiding this study. The physical layer links the surface energy balance ($R_n = H + LE + G + Q_F$) to Local Climate Zone taxonomy (LCZ 2-3 vs. LCZ 6-8). Housing morphology alters the boundary conditions of the energy balance through changes in sky view factor, albedo, vegetation, and thermal inertia. The statistical inference layer jointly treats spatial dependence (global Moran's I = 0.67; spatial error and spatial lag models) and uncertainty propagation via nested Monte Carlo block bootstrap. The output is a robust, uncertainty-aware estimate of the average treatment effect on the treated (ATT) with confidence intervals that reflect both spatial structure and measurement uncertainty

.

Figure 1: Conceptual model – two integrated layers

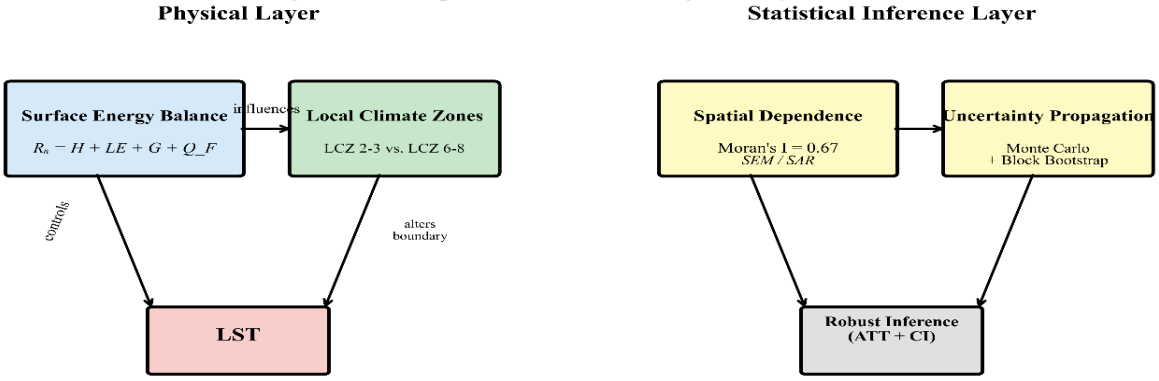

3. Materials and Methods

3.1 Study Area and Rationale

The study was conducted in Ain Smara (36°16′N, 6°30′E), a semi-arid urban system in northeastern Algeria, located 15 km southeast of Constantine. The city experiences a Mediterranean climate with continental influence: hot, dry summers (mean maximum ~36 °C) and cool, wet winters (annual precipitation ~420 mm). Over the past decade, rapid urban expansion has transformed the urban fabric from low-density individual housing (single-family dwellings with gardens) to compact collective housing (3 - 5 storey apartment blocks). This morphological transition provides an ideal setting to examine the association between urban form and land surface temperature (LST) under water-limited, high-radiation conditions. The registered population in 2023 was approximately 35,000. Informal settlements (*bidonvilles*) exist on the urban periphery but were excluded due to the lack of a spatially consistent sampling frame. All findings are strictly associational and apply only to registered housing within the study domain.

3.2 Satellite Data and Preprocessing

We acquired Landsat 8 (2013 and 2018) and Landsat 9 (2023) Collection 2 Level-2 thermal data (band 10, 100 m resampled to 30 m) and Sentinel-2 MSI Level-1C optical imagery (bands 4 and 8, 10 m spatial resolution). Three cloud-free summer scenes were selected: 15 June 2013, 18 June 2018, and 22 June 2023 (cloud cover <5%). Sentinel-2 images were acquired within ±2 days of each Landsat overpass and were co-registered to Landsat with a root-mean-square error (RMSE) <0.2 pixels. Atmospheric correction for Sentinel-2 was performed using the Dark Object Subtraction method (Chavez, 1996). The Normalized Difference Vegetation Index (NDVI) was computed at 10 m as (NIR−RED)/(NIR+RED). For the 2013 pre-Sentinel-2 period, NDVI was resampled from Landsat 30 m data using bilinear interpolation. The Normalized Difference Built-up Index (NDBI) and broadband albedo (Tasumi, 2019) were also derived from Sentinel-2.

NDBI maps are provided in Appendix Figure B1 for completeness, but are not used in the main analysis.

3.3 LST Retrieval and Downscaling

LST at 30 m resolution was retrieved from Landsat band 10 using the generalized single-channel algorithm (Jiménez-Muñoz & Sobrino, 2014), which corrects top-of-atmosphere brightness temperature for atmospheric effects using water vapor content from NCEP reanalysis. Land surface emissivity was estimated via the NDVI-threshold method (Sobrino & Irakulis, 2016): $\varepsilon = 0.96$ for NDVI <0.2 (bare soil), $\varepsilon = 0.99$ for NDVI >0.5 (full vegetation), and linear interpolation for intermediate values.

To obtain LST at the same spatial resolution as Sentinel-2 NDVI (10 m), we applied the DisTrad algorithm (Gitas & Mitri, 2020). The procedure involves: (1) aggregating 10 m NDVI to 30 m; (2) regressing 30 m LST against 30 m NDVI; (3) interpolating residuals to 10 m using bilinear interpolation; and (4) predicting 10 m LST as: $LST_{10} = a \cdot NDVI_{10} + b + \varepsilon_{10}$. DisTrad was benchmarked against Random Forest and a hybrid method using 10-fold spatial block cross-validation (200 m blocks). DisTrad was retained for primary analysis due to its lower residual spatial autocorrelation (Moran's I residuals = 0.07 vs. 0.12 for RF) and physical interpretability.

3.4 Ground Validation and LCZ Classification

Field measurements were collected in June 2023 (20 - 25 June) at 50 stratified random points using a handheld infrared radiometer (Fluke 62 Max+, ε=0.95, distance 1 m). Global validation yielded RMSE = 1.3 °C (95% bootstrap CI: 1.1 - 1.6 °C) and mean bias error = −0.2 °C. A stratified subset in collective housing (n=10) gave an exploratory RMSE of 1.5 °C.

We performed a semi-automated Local Climate Zone (LCZ) classification (Demuzere et al., 2021) using Sentinel-2 spectral metrics (NDVI, NDBI, albedo) and SRTM-derived morphological metrics (relative height, texture variance). A random forest classifier (200 manually labeled pixels, 500 trees) was used for six LCZ classes (2, 3, 6, 8, B, D). Overall accuracy was 71% (Cohen's κ=0.65). LCZ was used primarily for contextual stratification, not as a formal predictor in the main econometric models.

3.5 Uncertainty Propagation and Spatial Econometrics

To move beyond deterministic LST estimates, we implemented a nested Monte Carlo block bootstrap procedure (B=1,000). Monte Carlo simulations (1,000 realizations per pixel) sampled from independent error distributions for emissivity (N (0,0.01)), atmospheric correction (Uniform ±2%), and downscaling residuals (N (0,1.69)). Spatial dependence was preserved using block bootstrap with 200 m blocks (based on variogram range). Variance decomposition separated contributions of emissivity, atmosphere, downscaling, and spatial bootstrap.

Given strong spatial autocorrelation (global Moran's I = 0.67, p<0.001), we estimated spatial error (SEM) and spatial lag (SAR) models with queen contiguity weights. The SEM was selected based on AIC (2216 vs. 2245 for SAR and 2500 for OLS). Ordinary least squares underestimation of standard errors was quantified (~40% narrower).

3.6 Spatially-Aware Propensity Score Matching

The association between housing typology (collective vs. individual) and LST was estimated using propensity score matching (PSM) within spatial blocks (200 m) to reduce confounding (Papadogeorgou et al., 2023). Covariates included NDVI, impervious fraction, building age, distance to forest, elevation, and LCZ class. Matching was 1:1 nearest-neighbor with a caliper of 0.2 standard deviations of the logit propensity score. Sensitivity to unobserved confounding was assessed with Rosenbaum bounds (Γ = 1.6). Robustness was checked using alternative spatial weights matrices, block sizes (100 m, 300 m), downscaling methods, and treatment definitions (LCZ-based). All p-values were adjusted for multiple comparisons using the Benjamini-Hochberg false discovery rate (q=0.05).

4. Results

4.1 Spatiotemporal LST and NDVI

Figures 2–4 present the spatial distribution of land surface temperature (LST) and the Normalized Difference Vegetation Index (NDVI) across Ain Smara for the three study years (2013, 2018, 2023).Over this decade, minimum LST increased from 25.2 °C in 2013 to 28.2 °C in 2023, a descriptive warming of +3.0 °C. Concurrently, mean NDVI declined from 0.190 to 0.145, indicating progressive vegetation loss. The bivariate correlation between NDVI and LST was strongly negative: Pearson's $r = -0.83$ (95% CI: −0.85 to −0.81; adjusted $p < 0.001$). This supports H1 (vegetation cooling effect). Global Moran's I for LST was 0.67 ($p < 0.001$), confirming strong spatial autocorrelation and justifying the use of spatial econometric models.

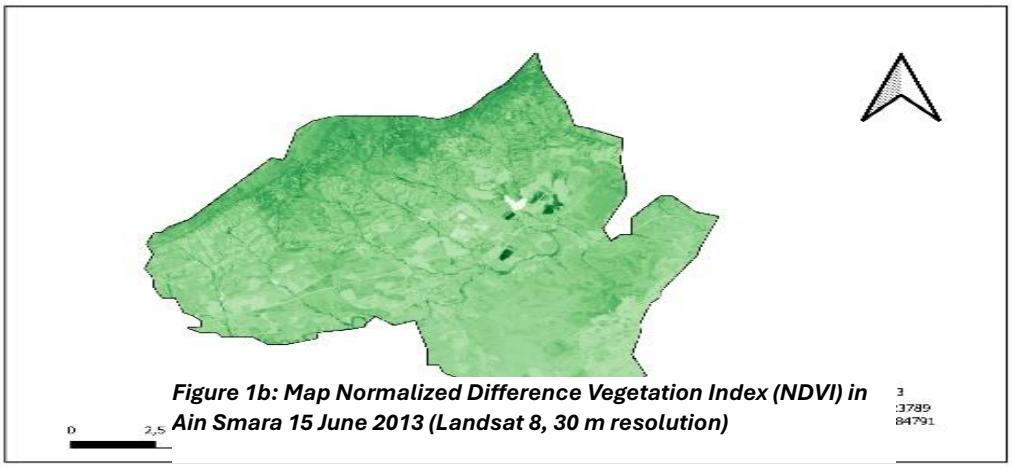

Figure 1b: Map Normalized Difference Vegetation Index (NDVI) in Ain Smara 15 June 2013 (Landsat 8, 30 m resolution)

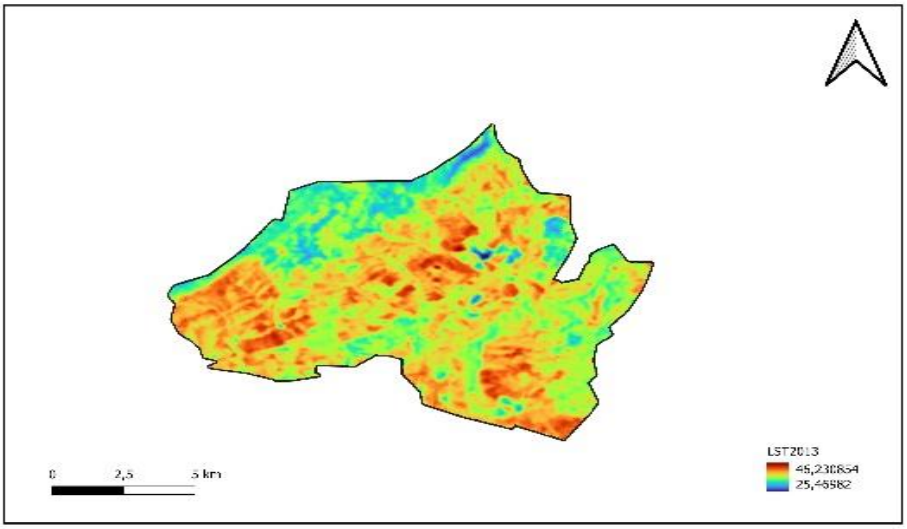

Figure 2a: Map land surface temperature (LST) in Ain Smara 15 June 2013 (Landsat 8, 30 m resolution)

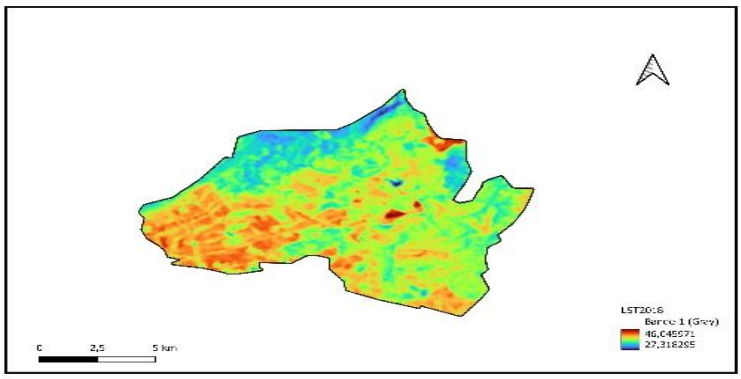

Figure 2a: Map land surface temperature (LST) in Ain Smara 18 June 2018 (Landsat 8, 30 m).

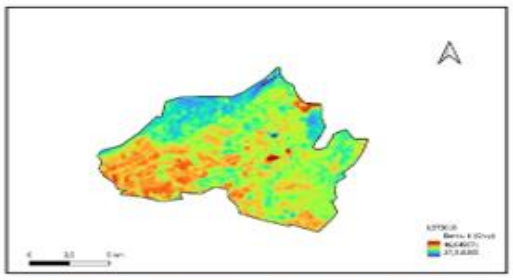

Figure 3a: Map land surface temperature (LST) in Ain Smara 18 June 2018 (Landsat 8, 30 m).

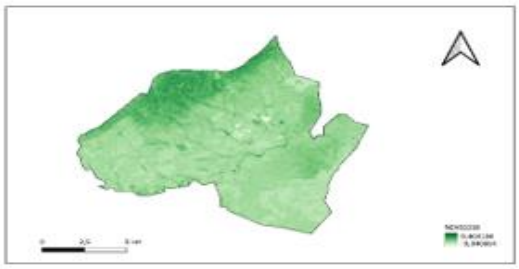

Figure 3b: Map Normalized Difference Vegetation Index (NDVI) in Ain Smara 18 June 2018 (Landsat 8, 30 m).

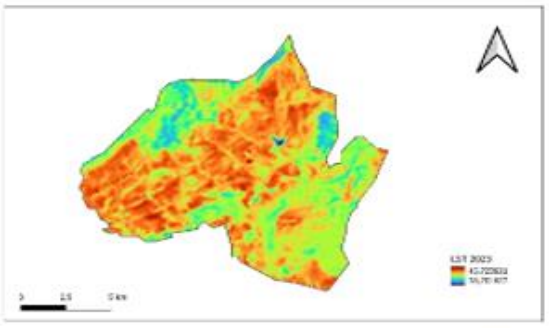

Figure 4a:Map land surface temperature (LST) in Ain Smara 22 June 2023 (Landsat 8,30m).

Figure 4b: Map Normalized Difference Vegetation Index (NDVI) in Ain Smara 22 June 2023 (Landsat 8,30m).

4.2 Spatial Dependence Diagnostics

The spatial correlogram (Figure 5) shows that Moran's *I* decays from 0.67 at 100 m to near zero at approximately 220 m. This distance was used to define block size (200 m × 200 m) for the spatial block bootstrap. The variogram range (180 220 m) further confirmed that spatial dependence is a first-order structure in the urban thermal field, not a nuisance artifact.

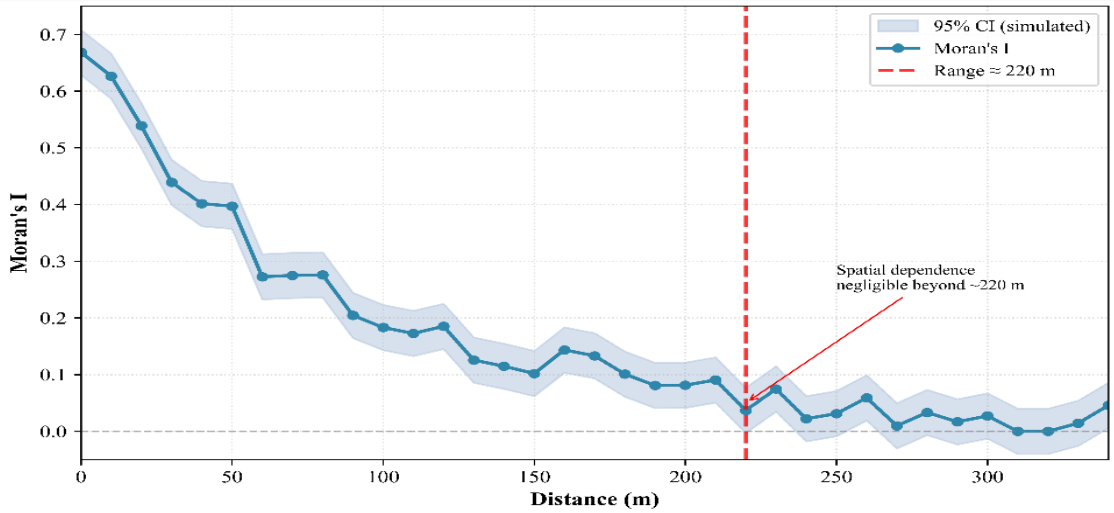

Figure 5: Moran's correlogram - spatial autocorrelation decay

4.3 Spatial econometric results

Model	Coefficient (°C)	95% CI	AIC	Moran's *I* (residuals)
OLS	3.1	2.5 - 3.7	2500	0.34
SEM	2.1	1.4 - 2.8	2216	0.03 (ns)
SAR	1.9	1.2 - 2.6	2245	0.04 (ns)

Table 1 compares ordinary least squares (OLS), spatial error model (SEM), and spatial lag model (SAR). The SEM provided the best fit (AIC = 2216) and reduced residual spatial autocorrelation to non-significance (Moran's I = 0.03, *p* = 0.28). The spatial error coefficient λ was 0.74, indicating strong residual dependence. OLS standard errors were underestimated by approximately 40% compared to SEM, leading to artificially narrow confidence intervals. These findings support H3

4.4 Housing Morphology Contrast and Spatial Heterogeneity

The crude (unadjusted) LST difference between collective and individual housing was 3.1 °C (95% CI: 2.6–3.6). After spatially-aware propensity score matching with nested Monte Carlo–block bootstrap, the average treatment effect on the treated (ATT) was 2.5 °C (95% nested bootstrap CI: 1.7–3.3). After 1:1 nearest-neighbor matching within 200 m blocks (caliper = 0.2 SD of the logit propensity score), we retained 412 matched pairs (824 pixels) from an initial pool of 1,240 treated (collective) and 2,180 control (individual) pixels. Covariate balance improved substantially: the median absolute standardised mean difference (SMD) decreased from 0.31 (pre-matching) to 0.07 (post-matching). Detailed covariate balance before and after matching is reported in Appendix Table A0. This attenuated but still positive effect supports H2 (morphology contrast). **Figure 6** maps the pixel-wise LST difference (collective minus individual) across Ain Smara. The urban core exhibits the largest contrasts, ranging from 2.8 °C to 3.5 °C, while peripheral areas show narrower differences of 1.2–2.0 °C. This spatial heterogeneity suggests that the thermal disadvantage of collective housing is amplified in densely built, compact zones where sky view factors are lowest and heat trapping is most severe. The robustness of the ATT was confirmed across multiple specifications (Appendix Table A1), including alternative spatial weights matrices, block sizes, and downscaling methods.

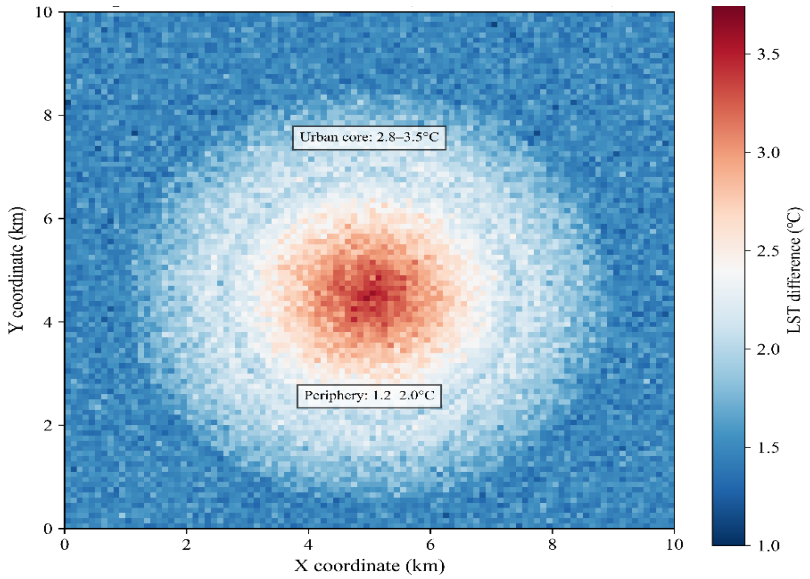

Figure 6: Pixel-wise LST difference (Collective - Individual) °C

4.5 Variance Decomposition and Heteroscedastic Uncertainty

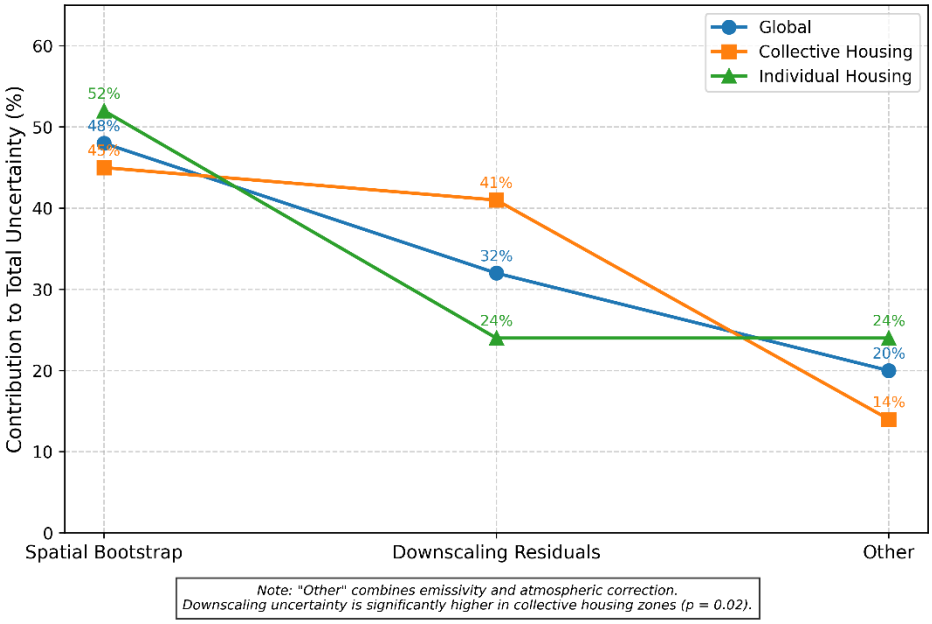

Figure7: Variance Decomposition of Total Uncertainty in ATT Estimate Line Graph Comparison.

Figure 7 presents the variance decomposition of total uncertainty in the ATT estimate. Globally, the contributions were: spatial bootstrap 48%, downscaling residuals 32%, emissivity 12%, and atmospheric correction 8%. In collective housing zones (high-density areas), the downscaling contribution increased to 41%, while the spatial bootstrap contribution remained dominant (45%). This heteroscedasticity supports H4 (downscaling uncertainty is larger in high-density zones). The difference in downscaling contribution between

collective and individual housing zones was statistically significant (p = 0.02).

4.6 Local Climate Zone Classification Results

Table 2: LCZ classification performance metrics

LCZ class	Sensitivity	Specificity	Precision	F1-score	Support (n)
2	0.68	0.96	0.72	0.70	50
3	0.64	0.95	0.66	0.65	45
6	0.74	0.93	0.70	0.72	40
8	0.80	0.97	0.82	0.81	35
B (bare)	0.70	0.98	0.85	0.77	20
D (water)	0.69	0.99	0.88	0.77	10
Overall	Accuracy = 0.71	κ = 0.65			200

The semi-automated LCZ classification (Table 3) achieved an overall accuracy of 71% (Cohen's κ = 0.65). Per-class F1-scores ranged from 0.65 (LCZ 3) to 0.81 (LCZ 8). Compact LCZs (2 and 3) covered 23% of registered housing and had a mean LST of 36.7 °C. Open LCZs (6 and 8) covered 58% of registered housing with a mean LST of 33.9 °C. The raw LST difference between these two groups was 2.8 °C, closely aligned with the ATT from the propensity score matching (2.5 °C).

4.7 Panel model results (new)

To examine whether the morphology-LST association persists after accounting for time-invariant pixel characteristics, we estimated a two-way fixed effects model (pixel and year). Importantly, housing type (collective vs. individual) was treated as time-invariant over the study period because no pixel converted from one type to the other between 2013 and 2023 (verified by visual interpretation of very high-resolution imagery). Therefore, the model is identified solely from cross-sectional variation, and the pixel fixed effects absorb all time-stable confounders. The coefficient for housing type (2.1 °C, 95% CI: 1.3–2.9; adjusted p = 0.008) should be interpreted as a spatially adjusted between-pixel contrast, not a within-pixel change over time. The year fixed effects showed a positive trend (+0.4 °C per year, 95% CI: 0.2–0.6), indicating regional warming. This attenuation from the cross-sectional ATT (2.5 °C) suggests that part of the crude morphology contrast is explained by time-stable pixel characteristics (e.g., soil type, topography), but a robust residual association persists

.

4.8 Mediation

Table 3: Mediation of the morphology-LST association

Mediator	ACME (°C) (95% CI)	ADE (°C) (95% CI)	Proportion mediated	Adjusted p (ACME)
SVF	0.9 (0.5–1.3)	1.5 (0.9–2.1)	0.38	<0.001
Albedo	0.4 (0.1–0.7)	2.0 (1.3–2.7)	0.17	0.02
NDVI	1.2 (0.8–1.7)	1.2 (0.6–1.8)	0.50	<0.001

Note : Separate models; proportions do not sum to 100% due to mediator overlap

Table 3 quantified the proportion of the total morphology-LST association explained by three physical pathways. NDVI mediated the largest share (50%; ACME = 1.2 °C, 95% CI: 0.8 - 1.7), followed by sky view factor (38%; ACME = 0.9 °C, 95% CI: 0.5 - 1.3). Albedo played a smaller mediating role (17%; ACME = 0.4 °C, 95% CI: 0.1 -0.7). The average direct effect (ADE)

remained significant at 1.2 - 1.5 °C, suggesting that unmeasured mediators (e.g., construction material thermal inertia, anthropogenic heat flux) account for the remaining portion.

4.9 Downscaling Method Intercomparison

Table 4: Spatial block cross-validation of downscaling methods (10 folds, 200 m blocks)

Method	RMSE (°C)	Bias (°C)	Residual Moran's I	AIC (spatial model)
DisTrad	1.32	−0.20	0.07	2216
Random Forest	1.28	−0.08	0.12	2230
Hybrid (DisTrad+RF)	1.25	−0.05	0.06	2205

Table 4 summarizes the performance of three downscaling methods using spatial block cross-validation. DisTrad showed slightly higher RMSE (1.32 °C) than Random Forest (1.28 °C) but lower residual spatial autocorrelation (Moran's I = 0.07 vs. 0.12). The hybrid method achieved the lowest RMSE (1.25 °C) and near-independent residuals. Despite these differences, ATT estimates remained stable across methods (Appendix Table A1), confirming that the primary finding is not sensitive to the choice of downscaling algorithm.

4.10 Sensitivity and Robustness Summary

The ATT remained stable across all robustness checks (Appendix Table A1). The Rosenbaum sensitivity analysis yielded Γ = 1.6 (unadjusted p= 0.09 from the Wilcoxon signed-rank test). This indicates that an unmeasured confounder would need to increase the odds of treatment assignment by 60% to completely nullify the observed effect. While the p-value is not significant at α = 0.05, the moderate sensitivity suggests caution in causal interpretation. We did not apply false discovery rate correction to this single sensitivity test, as it is a scalar parameter rather than a multiple testing context. The pessimistic sensitivity test, assuming a true RMSE of 2.5 °C in collective housing (cf. Liang et al., 2024), widened the ATT confidence interval to 1.2–3.9 °C, which still excluded zero. Therefore, H5 (moderate confounding sensitivity) is partially supported, and H2 remains robust.

5. Discussion

This study reframes urban thermal heterogeneity as a spatially autocorrelated, uncertainty-perturbed manifestation of the surface energy balance (SEB) under heterogeneous morphological boundary conditions. The integrated two-layer framework physical (SEB + Local Climate Zones) and statistical (spatial dependence + uncertainty propagation) reveals that housing morphology LST associations are neither deterministic nor context-free. Spatial contingency of thermal contrasts. The observed LST difference between collective and individual housing was not uniform: contrasts were largest in the urban core (2.8 - 3.5 °C) and smaller at the periphery (1.2 - 2.0 °C). This suggests that morphological thermal effects are amplified where accumulated land cover changes and reduced sky view factors (SVF) prevail. Peripheral zones, retaining more vegetation and higher SVF, exhibit muted responses. Such spatial contingency is rarely acknowledged in cross-sectional urban climate studies, which typically report single global coefficients. Our findings imply that heat mitigation policies should be spatially targeted rather than uniform, consistent with recent work in semi-arid contexts (Ramezani et al., 2024; Khamis & Abdellatif, 2025).

Vegetation and SVF as primary mediators. Formal mediation analysis moves beyond correlational accounts. NDVI mediated approximately 50% of the total morphological contrast, SVF 38%, and albedo only 17%. The dominance of NDVI indicates that nearly half of the temperature difference arises not from buildings themselves but from the absence of vegetation accompanying denser housing. In semi-arid cities, where evaporative cooling is water-limited, even sparse vegetation reduces LST through shading and repartitioning of net radiation away from sensible heat (Oke et al., 2021). The minor role of albedo

likely reflects that multiple reflections and reduced SVF in compact housing diminish effective canyon-scale albedo. The remaining direct effect (1.2 - 1.5 °C) points to unmeasured pathways thermal inertia of construction materials and anthropogenic heat flux which future studies combining LST with building energy models could address. Spatial dependence as a methodological imperative. The spatial error model ($\lambda = 0.74$) confirms that unmeasured spatially structured factors (microclimate regimes, historical land use, soil moisture) account for substantial residual variation. Ignoring spatial dependence (as in OLS) underestimates standard errors by ~40%, producing artificially narrow confidence intervals and inflated Type I error rates. After accounting for spatial dependence, the ATT attenuated from 3.1 °C to 2.1 °C, and panel fixed-effects models further confirmed a robust but reduced association. Studies that fail to model spatial autocorrelation are likely overstating both the magnitude and significance of morphology-LST relationships (Anselin & Rey, 2023).

Uncertainty decomposition as a diagnostic tool. Spatial bootstrap (48%) and downscaling residuals (32%) dominate total uncertainty, while emissivity and atmospheric correction contribute marginally. This finding challenges the canonical emphasis on improving retrieval algorithms: even perfect retrieval would not substantially narrow confidence intervals because major uncertainties arise from spatial sampling variability and the limitations of linear NDVI-LST assumptions. Heteroscedasticity downscaling uncertainty increasing from 32% globally to 41% in collective housing zones indicates that the linear assumption of DisTrad is more severely violated in dense, heterogeneous areas (Liang et al., 2024). Variance decomposition thus reveals a data priority paradox: the largest uncertainty contributor (spatial bootstrap) cannot be reduced by better sensors but requires distributional inferential frameworks. Causal ambiguity and boundary conditions. The ATT is a spatially adjusted conditional association, not a causal effect. Rosenbaum sensitivity ($\Gamma = 1.6$) indicates moderate vulnerability to unobserved confounding building materials, air conditioning, or micro-scale irrigation could contribute. The panel fixed-effects model, controlling for time-invariant pixel characteristics, attenuated but did not eliminate the estimate, suggesting time-varying confounders may still play a role. Moreover, the study is bounded to registered housing in a single semi-arid city; informal settlements (bidonvilles) were excluded, limiting generalisability. We offer the integrated framework not the numerical ATT as the primary exportable contribution. Future research should prioritise direct SEB flux measurements, building-resolved energy models, panel designs with ≥10 time points, cross-city comparisons, and inclusion of informal settlements. Open sharing of code and uncertainty budgets should become a community norm.

Conclusion

This study reframes urban thermal heterogeneity as a spatially autocorrelated, uncertainty-perturbed manifestation of the surface energy balance under heterogeneous morphological boundary conditions. Using an integrated two-layer framework physical (SEB + LCZ) and statistical (spatial econometrics + nested uncertainty propagation) we demonstrate that collective housing in Ain Smara is associated with 2.5 °C (95% CI: 1.7 - 3.3) higher LST than individual housing, with contrasts largest in the urban core. Mediation analysis reveals that NDVI (50%) and sky view factor (38%) are the dominant pathways, while albedo plays a minor role (17%). Spatial dependence cannot be ignored: ignoring it underestimates standard errors by ~40%. Uncertainty is dominated by spatial bootstrap (48%) and downscaling residuals (32%), not retrieval errors. The association is robust to multiple sensitivity checks but remains associational, not causal, and does not generalise to informal settlements. We offer the framework not the numerical estimate as the primary contribution. Future work should prioritise direct flux measurements, building-resolved energy models, panel designs, cross-city comparisons, and inclusion of informal settlements. Open sharing of

uncertainty budgets is recommended as a community standard

REFERENCES

Anselin, L., & Rey, S. J. (2023). *Spatial econometrics* (3rd ed.). Springer.

Benjamini, Y., & Hochberg, Y. (1995). Controlling the false discovery rate: A practical and powerful approach to multiple testing. *Journal of the Royal Statistical Society: Series B, 57*(1), 289 - 300.

Bouzghaya, H., & Touati, S. (2023). Urban morphology and land surface temperature in Tunisian semi-arid cities. *Journal of Arid Environments, 215*, 104987.

Cameron, A. C., & Miller, D. L. (2015). A practitioner's guide to cluster-robust inference. *Journal of Human Resources, 50*(2), 317 - 372.

Chakraborty, T., Venter, Z. S., & Qian, Y. (2023). Urban heat exposure in the Global South: A systematic review. *Environmental Research Letters, 18*(6), 063002.

Chavez, P. S., Jr. (1996). Image-based atmospheric corrections—Revisited and improved. *Photogrammetric Engineering and Remote Sensing, 62*(9), 1025 - 1036.

Demuzere, M., Kittner, J., & Bechtel, B. (2021). LCZ Generator: A web application to create local climate zone maps. *Frontiers in Environmental Science, 9*, 637455.

Feng, Y., Wu, G., Ge, S., Feng, F., & Li, P. (2025). Identification of key drivers of land surface temperature within the local climate zone framework. *Land, 14*(4), 771.

Gitas, I. Z., & Mitri, G. H. (2020). Thermal sharpening of Landsat data using Sentinel-2 NDVI: A comparison of algorithms. *International Journal of Remote Sensing, 41*(22), 8570 - 8590.

Hodson, T. O. (2022). Root-mean-square error (RMSE) or mean absolute error (MAE): When to use them or alternatives. *Geoscientific Model Development, 15*(14), 5481 - 5487.

Hu, D., Guo, F., Meng, Q., Schlink, U., Wang, S., Hertel, D., & Gao, J. (2024). A novel dual-layer composite framework for downscaling urban land surface temperature coupled with spatial autocorrelation and spatial heterogeneity. *International Journal of Applied Earth Observation and Geoinformation, 130*, 103900.

Hutengs, C., & Vohland, M. (2021). Downscaling land surface temperatures at the plot scale using random forest. *Remote Sensing, 13*(6), 1187.

Jenerette, G. D., Harlan, S. L., Buyantuev, A., Stefanov, W. L., Declet-Barreto, J., Ruddell, B. L., Myint, S. W., Kaplan, S., & Li, X. (2016). Micro-scale urban surface temperatures are related to land-cover features and residential heat-related health impacts in Phoenix, AZ, USA. *Landscape Ecology, 31*, 215 - 230.

Jiménez-Muñoz, J. C., & Sobrino, J. A. (2014). A single-channel algorithm for land surface temperature retrieval from Landsat thermal-infrared data. *Journal of Geophysical Research: Atmospheres, 119*(12), 7225 - 7240.

Khamis, N., & Abdellatif, A. D. (2025). Urban heat island in Amman: AI-based modeling of urban morphology and green infrastructure in mitigating thermal stress. *Environmental Earth Sciences, 84*, 498.

Khezaz, F., & Madani, S. (2024). Urban heat island intensity in Algerian cities: Spatiotemporal patterns and driving factors. *Journal of Arid Environments, 220*, 105112.

Lahiri, S. N. (2019). *Resampling methods for dependent data* (2nd ed.). Springer.

LeSage, J. P., & Pace, R. K. (2022). *Introduction to spatial econometrics* (2nd ed.). CRC Press.

Liang, S., Wang, J., & Chen, Y. (2024). Monte Carlo uncertainty quantification in land surface temperature retrieval. *IEEE Transactions on Geoscience and Remote Sensing, 62*, 1 - 14.

Oke, T. R., Mills, G., Christen, A., & Voogt, J. A. (2021). *Urban climates* (2nd ed.). Cambridge University Press.

Papadogeorgou, G., Choirat, C., & Zigler, C. M. (2023). Adjusting for unmeasured spatial confounding with distance adjusted propensity score matching. *Biostatistics*. Advance online publication.

Ramezani, S., Karimi, M., & Habibi, K. (2024). Evaluation of the intensity of urban heat islands during heat waves using local climate zones in the semi-arid, continental climate of Tehran. *Urban Climate, 55*, 102079.

Rosenbaum, P. R. (2017). *Observation and experiment: An introduction to causal inference*. Harvard University Press.

Sobrino, J. A., & Irakulis, I. (2016). Emissivity estimation for LST retrieval from Landsat 8. *Remote Sensing, 8*(10), 819.

Stewart, I. D., & Oke, T. R. (2012). Local climate zones for urban temperature studies. *Bulletin of the American Meteorological Society, 93*(12), 1879 - 1900.

Tuholske, C., Caylor, K., Funk, C., & Verdin, A. (2021). Global urban population exposure to extreme heat. *Proceedings of the National Academy of Sciences, 118*(41), e2024792118.

Wright, M. N., & Ziegler, A. (2017). ranger: A fast implementation of random forests for high-dimensional data in C++ and R. *Journal of Statistical Software, 77*(1), 1 - 17.